Aerospace Science and Technology xxx (xxxx) 109641

Contents lists available at ScienceDirect

Aerospace Science and Technology

journal homepage: www.elsevier.com

Journal logo

Integration of the passive energy balancing based actuation system into a camber morphing design

C. Wang [a], Y. Zhao [a], K. Huang [b], J. Zhang [b,*], A.D. Shaw [c], H. Gu [d], M. Amoozgar [e], M.I. Friswell [c], B.K.S. Woods [d]

[a] College of Aerospace Engineering, Nanjing University of Aeronautics and Astronautics, China
[b] School of Aeronautic Science and Engineering, Beihang University, China
[c] Faculty of Science and Engineering, Swansea University, United Kingdom
[d] Department of Aerospace Engineering, University of Bristol, United Kingdom
[e] Department of Mechanical, Materials & Manufacturing Engineering, University of Nottingham, United Kingdom

ARTICLE INFO

Keywords:
Passive energy balancing
Morphing wing
Energy efficiency
Tuned stiffness

ABSTRACT

A spiral pulley mechanism can be used to passively balance the energy between the morphing structure and actuation system. Applying the energy balancing concept has the potential to improve the performance of the actuation system by reducing the external energy consumption. In the current study, the integration workflow for the passive energy balancing device is established and is adopted in a variable camber morphing wing. The design variables of the passive energy balancing system are optimised and the effects of the different parameters are discussed together with the adaptability of the passive energy balancing device when the load stiffness changes. An integrated demonstrator was also built to validate the mechanism by measuring the currents in the process of morphing actuation.

Nomenclature

E_o	energy output by the spiral pulley mechanism
E_r	energy required for morphing
E_x	external energy requirement of passive energy balancing device
g	gear ratio between the load pulley and spiral pulley
J_n	normalized energy requirement
$k_{1,2}$	spiral pulley geometry parameters
k_{drive}	drive spring rate
k_l	load stiffness
L_0	drive spring pre-extension
r_0	spiral pulley initial radius
T_d	drive torque
T_l	load torque
x_{off}	x-axis offset of the spiral coordinate origin
y_{off}	y-axis offset of the spiral coordinate origin
δ_0	Initial spiral pulley rotation angle

FishBAC	FishBAC Bone Active Camber
PEB	Passive Energy Balancing
SPNS	Spiral Pulley Negative Stiffness

1. Introduction

An actuation system is an essential part of any potential morphing aircraft and rotorcraft concept. The actuation system needs to provide adequate force and stroke output while minimizing the weight and cost. The increase of weight and energy consumption caused by the actuation system could negate the morphing benefits and lead to reduced overall performance. When the shape change requires elastic deformation of morphing structures, the actuation system needs to provide the elastic strain energy during each shape-changing cycle, which will be dissipated as the energy is not recycled in the system, resulting in excessive energy requirements and weight penalties due to oversize actuators.

* Corresponding author.
E-mail address: jiaying.zhang@buaa.edu.cn (J. Zhang).

https://doi.org/10.1016/j.ast.2024.109641
Received 12 March 2024; Received in revised form 14 September 2024; Accepted 29 September 2024
1270-9638/

Different types of actuators have been proposed to satisfy the high demand of the actuation energy. Conventional actuation methods, such as hydraulic actuation and servo motors, are still often applied in morphing [1]. Smart materials, such as shape memory alloys and polymers, and piezoelectric materials [2–4], can be applied to introduce new design approaches for morphing aircraft and rotorcraft, although they may require high actuation voltage [5] or have a low actuation bandwidth [6]. Optimisation of the morphing structure as well as the actuation layout can be performed to achieve an improved actuation efficiency. In the camber morphing wing design proposed by DiPalma and Gandhi [7], the region aft the spar was made very stiff to reduce the deformation under aerodynamic loads, while lower stiffness was applied in the reverse direction to reduce the actuation load. Rigid cantilevers, which extended from the rear part of the spar to the trailing edge of the aerofoil, were added into the aerofoil structure to achieve the variable stiffness. A gripper pin structure was proposed by You et al. [8] to decouple the in-plane and out-of-plane stiffness of the morphing skin, which would allow shape change and require low actuation energy simultaneously. In addition to the structural optimisation, the actuation system can also be optimised to improve the efficiency of morphing aircraft. A distributed actuation system for the scissor type structure was investigated using a multi-disciplinary optimisation by Westfall et al. [9]. The optimised locations and orientations of the actuators were found to improve the efficiency of the actuation system. The layout of the distributed piezoelectric actuators were optimised to achieve performance improvement by Henry et al. [10]. Bistable and multistable structures can reduce the actuation energy consumption, as they only requires actuation to induce the snap-through of the structure rather than for the entire operation process [11,12]. Multistable composites were used in a morhphing trailing edge design by Haldar et al. [13]. Multistable composite plates were driven by a piezoelectric actuator and the location of the actuator was optimised to increase the displacement of the trailing edge while keeping the actuation voltage modest. A pressure-based actuation system was also used in the morphing wingtip structures by Meyer, Traub and Hühne [14] since the pressure can be used to tune the stiffness of the structure adaptively. Shape memory polymer has been applied as the skin of the structure, which can provide an aerodynamic surface and also tune the stiffness, by Sun et al. [15]. However, whatever the actuator is selected, the structure stiffness cannot be changed by the actuator, and the requirement of the actuation energy will remain at a demanding level.

Alternatively, an actuation system based on the passive energy balancing (PEB) concept has the potential to reduce the energy consumption requirement inherently. Rather than simply increasing the output energy from the actuator, the actuation energy is stored within the system to drive the morphing structure. The entire system consists of the actuation mechanism and the morphing structure, and is balanced. The stored energy, which is released by the elastic structure, can be recycled in the system, if friction and non-elastic deformations are negligible.

In the authors' earlier research [16,17], a morphing wingtip based on compliant structures was proposed and optimised to reduce the required actuation force and improve the performance of the aircraft. The passive energy balancing concept based on a negative stiffness mechanism, which gives a significant energy saving with a small weight penalty [18]. In this paper, the spiral pulley negative stiffness (SPNS) mechanism is applied to balance the Fish Bone Active Camber (FishBAC) morphing concept [19–21]. The spiral pulley has a spooling cable, which is connected to a pre-stretched spring. The spiral pulley is a key feature to improve the actuation performance compared to the circular spooling pulley, as it can generate a torque-rotation curve that is very similar to the required one [22]. The rotation of the spiral pulley can release the energy stored in the spring and deform the morphing structure. Due to the geometric configuration of the spiral pulley and the kinematic tailoring it provides, 'negative' stiffness is generated, which will balance the 'positive' stiffness of the morphing structure [23]. There has been extensive research on 'zero-stiffness' concepts, obtained through different working principles and used for different applications. In the field of vibration isolation, 'quasi-zero-stiffness' devices have been used as isolators, which give zero dynamic stiffness [24,25]. On the other hand, a structure with zero static stiffness can also be realised by an appropriate combination of stiffness, geometry and prestress [26]. These structures can undergo large elastic deformation without consuming external energy. Tensegrity structures, which are based on tension members with a zero rest length 27, and shell structures with a particular geometry and initial stress 28, are two examples of zero static stiffness structures given by Guest et al. [27, 28].

While our previous studies have demonstrated the spiral pulley based concept in desktop demonstrators [29,30], it has not previously been integrated in a true morphing wing structure with the aerodynamic shape. Limited space in the aerofoil raises challenges in terms of the design and manufacturing. Moreover, the current study will investigate the adaptability of the passive energy balancing (PEB) device when it is subject to different load stiffnesses. The different load stiffnesses can be caused by the replacement of the morphing structure, and the uncertainties in the process of manufacturing and assembly. Rather than pursuing purely zero stiffness, the proposed PEB device is more focused on the potential to reduce the external energy requirement. From the perspective of energy balancing, the energy to deform the structure can be provided from the external actuator and the internal drive spring. Thus, the external energy requirement is the real performance criteria of the PEB device rather than the stiffness. As a negative stiffness element, the spiral pulley together with the drive spring, can reduce the required external energy, even if the overall stiffness is not zero. The spiral pulley mechanism is able to generate torque that matches the required torque of the morphing system closely. Thus, a significant contribution can be provided by the negative stiffness mechanism to balance the positive stiffness system. The spiral pulley negative stiffness device can reduce the torque required to deform the structure by making use of the pre-stored energy, which can reduce the mass of the actuator and its auxiliary equipment.

The current research will evaluate the effect of the passive energy balancing device with the variation of the load stiffness and demonstrate the integration process for the FishBAC morphing wing structure. The model used in the paper is defined in Section 2 together with the workflow proposed. Preliminary evaluation is performed in Section 3, after which the optimisation of the spiral pulley mechanism is conducted in Section 4, which is followed by the demonstrator integration and experimental validation.

2. Model definition

2.1. Conceptual design

The integration concept is shown in Fig. 1. Fig. 1(a) shows the schematic of the FishBAC design driven by servo motors [20]. The torque generated by the servo motor is transferred to the FishBAC spine through two tendons attached to the solid trailing edge section. The tendons are made of KEVLAR (Tendon modulus 131 GPa), which is strong enough to drive the trailing edge of FishBAC prototype. A detailed analysis of the chordwise distribution of flexural rigidity has been performed, together with the FSI analysis, which validated the desired deformation under aerodynamic loads [15]. A PEB device using the bidirectional SPNS mechanism was firstly proposed in [30,31] as shown in Fig. 1(b). Two spiral pulleys are mounted onto one central shaft, and the bidirectional motion can be achieved through the rotation of the pulleys in opposite directions.

The parameters of the FishBAC design are listed in Table 1. The NACA23012 aerofoil is chosen for the integration, and the chord and span are 270 mm and 250 mm respectively. The current approach uses the cables from the load pulley as the tendons to drive the FishBAC

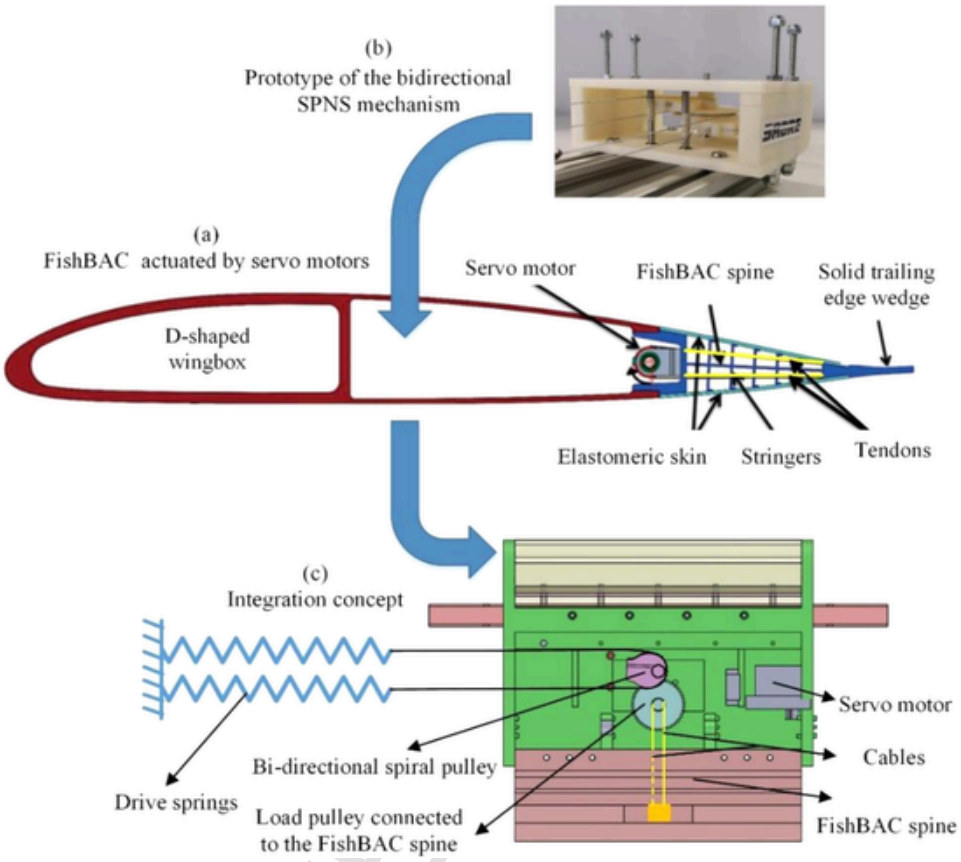

Fig. 1. (a) FishBAC driven by servo motors [20]; (b) Prototype of the bidirectional SPNS mechanism [30,31]; (c) Integration concept.

Table 1
FishBAC demonstrator parameters.

Parameter	Value
Baseline aerofoil	NACA 23012
Chord	270 mm
Span	250 mm
Start of morphing section	185 mm
End of morphing section	270 mm
Spine thickness	2 mm
Stringer thickness	0.8 mm
Skin thickness	1.5 mm
Tendon diameter	0.7 mm
Spine modulus	2.14 GPa
Stringer modulus	2.14 GPa
Tendon modulus	131 GPa
Skin modulus	4.56 GPa

spine directly, which simplifies the mechanism but can still demonstrate the potential of the spiral pulley. Fig. 1(c) shows the main components of the integrated morphing wing design. The spiral pulley and load pulley are installed into the FishBAC wing structure and the drive springs are connected to the fixed support, which can be the central wing box in the aircraft. A servo motor is used to drive the spiral pulley but the output torque required could be significantly reduced. Some of the connection wires are omitted to highlight the PEB mechanisms in the figure.

Fig. 2 shows the detailed designs of the spiral pulley and the load pulley. A cable is used to connect the spiral pulley and the drive spring. The cable is fixed into an installation hole in the spiral pulley. The load pulley, which will drive the FishBAC, is meshed with the spiral pulley through spur gears. Cables are also used to connect the load pulley and the FishBAC structure.

2.2. Mathematical definition

Fig. 3 shows the planar geometry of the spiral pulley and its rotation associated with the drive spring. The radius, r, about point O, which is the centre of the rotation shaft, can be defined as an exponential function

$$r = r_o + k_1 e^{k_2(\theta+\delta+\delta_o)} \tag{1}$$

where δ is the rotation angle of the spiral pulley, θ is an associated angle and δ_0 is the initial rotation angle. The parameters k_1, k_2 are the pre-exponent and exponent terms of the spiral pulley, which will determine the geometry of the spiral pulley together with the initial pulley radius r_0. As shown in Fig. 3, the coordinate offsets of the spiral pulley origin, x_{off} and y_{off}, are also needed to define the location of the spiral pulley.

The spiral pulley is connected to the drive spring, which has stiffness k_{drive}, and pre-tension determined by L_0. The spiral pulley is meshed with the load pulley with a gear train to transfer the torque to the FishBAC structure. The load pulley has cables connected to the FishBAC structure, and the drive torque output at the load pulley is given by

$$T_d = g \cdot F_d l_m \tag{2}$$

where g is the gear ratio, F_d is the force caused by the drive spring and l_m is the moment arm determined by the geometry feature and the rotation angle of the spiral pulley.

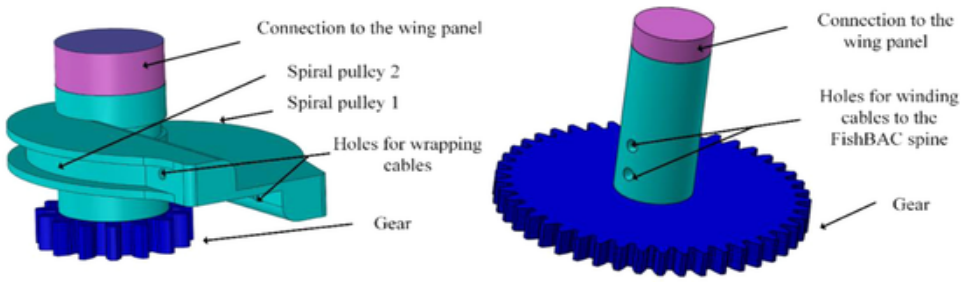

Fig. 2. Schematic of the spiral pulley with detailed designs.

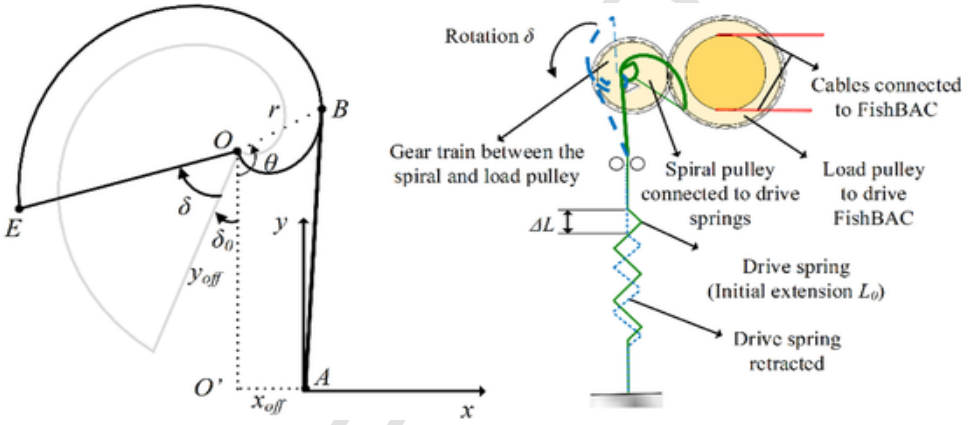

Fig. 3. Geometry of the spiral pulley and its connections to the FishBAC and drive springs.

The expression of the drive torque has been derived in [23,31]. The force, F_d, is a function of the rotation angle, the parameters of the spiral pulley geometry and the drive spring. The moment arm, l_m, varies with the rotation of the spiral pulley, and thus the drive torque is influenced by the geometry parameters of the spiral pulley, the drive spring stiffness and the initial extension.

In the previous study, the load torque T_l is a fixed function of rotation angle determined by the morphing structure. However, in the current study, the change of the load torque ΔT_l could be caused by the possible replacement of the morphing structure for different flight conditions and the uncertainties in the process of manufacturing and assembly.

If the load torque can be balanced by the drive torque partially or completely, less external energy will be consumed by the actuation system, as the energy stored in the drive spring can help to deform the structure. The stiffness corresponding to the load torque is called the load stiffness, and denoted as k_l in this paper.

The gear ratio between the spiral pulley and the load pulley is defined as $g = n_2/n_1$, and the number of teeth on the spiral pulley and the load pulley are denoted by n_1 and n_2 respectively. When the gear ratio is larger than 1, the drive torque output by the load pulley can be amplified, which can help to overcome high torque requirements. On the other hand, the rotation angle of the spiral pulley will be increased. The rotation range of the load pulley is determined by the FishBAC structural deformation, which means only a small fraction of the drive spring pre-extension will be used, and most of the stored energy cannot be used to balance the structural deformation. Adding the gears will increase the rotation range of the spiral pulley for the same structural deformation, and increase the efficiency of the passive energy balancing.

The performance of the passive energy balancing device is evaluated by the energy difference between the energy output of the spiral pulley mechanism and the energy required for FishBAC morphing [23], as the energy difference is inherently provided by the external actuator. The performance index E_x, which is the external energy requirement of the PEB device, is defined as

$$E_x = |E_o - E_r| \tag{3}$$

where the energy output by the spiral pulley system, E_o, and the energy required for FishBAC morphing, E_r, can be obtained through the integral of the drive torque T_d and the load torque T_l. For the same morphing requirement E_r, the performance index can also be normalized by the energy requirement E_r.

The application of the PEB device aims to reduce the external energy requirement. The normalised energy difference is adopted as the objective and given by

$$\min J_n = \frac{E_x}{E_r} = \frac{|E_o - E_r|}{E_r} \tag{4}$$

where min means the PEB device will be optimised to guarantee the difference between the energy output by the spiral pulley system and the energy required for FishBAC morphing is minimum, which means the energy stored by the PEB device will help to actuate the morphing structure through the spiral pulley mechanism and thus the external energy consumption, i.e., energy consumed by the servo motor in this case, can be reduced.

Obviously, the integrated spiral pulley and the load pulley should not have any geometric interference within the morphing structure. The space in a morphing structure is limited and will limit the maximum available size of the spiral pulley. The geometric constraints are written as

$$\begin{aligned} &r_{\max} < r_{\lim} \\ &N_s r_{\max} + N_l q < f_c \cdot C \\ &\max\left(h_s,\ h_l\right) < t_c \cdot C \end{aligned} \tag{5}$$

Here, the maximum radius of the spiral pulley r_{max} needs to be small enough to avoid any interference with the load pulley, especially considering the rotation of the spiral pulley. The radii of the spiral pulley and load pulley are denoted as r and q, and the coefficients N_s and N_l are factors to determine the maximum radii of the pulleys after the gears are added. As the spiral and load pulleys are within the aerofoil, the sum of their radii should be smaller than the chord. Also, the height of the spiral and load pulleys, h_s and h_l, should be lower than the aerofoil thickness. The chord is denoted as C and two ratios f_c and t_c, are used to represent the chordwise space the pulleys can occupy, and the thickness to chord ratio of the aerofoil. It should be noted that the maximum radius of the spiral pulley is constrained by the rotation range of the spiral pulley, as only part of the spiral pulley profile is used. The geometry constraint is checked for the preliminary evaluation and after the optimisation.

The related parameters are listed in Table 2. These parameters can be categorised as component-level parameters, i.e. the parameters to determine the spiral pulley geometry and the parameters of the drive spring, and the assembly level parameters, i.e. the gear ratio between the spiral and load pulley and the parameters to determine the installation position and initial orientation of the spiral pulley.

Table 2
Design parameters in the passive energy balancing device.

Parameter name	Parameter level
Initial radius, r_0	component level: spiral pulley geometry parameters
Pre-exponent term, k_1	
Exponent term, k_2	
Drive spring pre-extension, L_0	component level: drive spring
Drive spring rate, k_{drive}	
Drive spring initial force, F_0	
Gear ratio between the spiral pulley and the load pulley, g	assembly level: fixed parameter
Initial spiral pulley rotation angle, δ_0	assembly level: installation position and orientation of the spiral pulley
x-axis offset of the spiral coordinate origin, x_{off}	
y-axis offset of the spiral coordinate origin, y_{off}	

2.3. Workflow applied

In the process of integration, two major factors are taken into account:

1) The feasibility of the integrationThe first important factor is whether it is possible to apply the PEB device into the morphing wing. The main constraint is the limited space inside the aerofoil and the load path of the wing structure shall not be broken by the PEB device.
2) The efficiency of the integrated systemThe second important factor is whether the PEB device can reduce the external energy consumption, and to take a step further, whether the applied device has a good adaptability to work under different load stiffnesses.

With the two factors taken into consideration, the work flow applied in the current study is represented in Fig. 4.

Different to the earlier studies [22,29,30], the current work intends to show the adaptability of the PEB device, and the actuation energy can still be reduced even if the PEB device was not optimised for the changed structural stiffness. Thus, the design variables are not optimised simultaneously in a single step. And the actuation energy can still be reduced by only tuning the parameters of the drive spring and (or) the offsets.

The design inputs include the FishBAC demonstrator parameters as listed in Table 1, the possible load conditions and the candidate spiral pulleys that have been obtained in previous research. As shown in Fig. 2, significant detailed design work for the spiral pulley is required after obtaining the spiral pulley parameters. Considering the cost of a manufacturing and design iteration and the possible change of the load stiffness, it is necessary to consider the adaptability of the spiral pulley mechanism for different cases.

The first step is the preliminary evaluation. The geometry of the existing spiral pulleys will be checked to find whether the size of the spiral pulley can satisfy the geometry constraint of the demonstrator. The load stiffness, under which the spiral pulley was optimised, will also be evaluated to find whether it is within the potential working range of the load stiffnesses. If the candidate spiral pulley can be compatible, the existing spiral pulley will be selected for the next step. Otherwise, optimi-

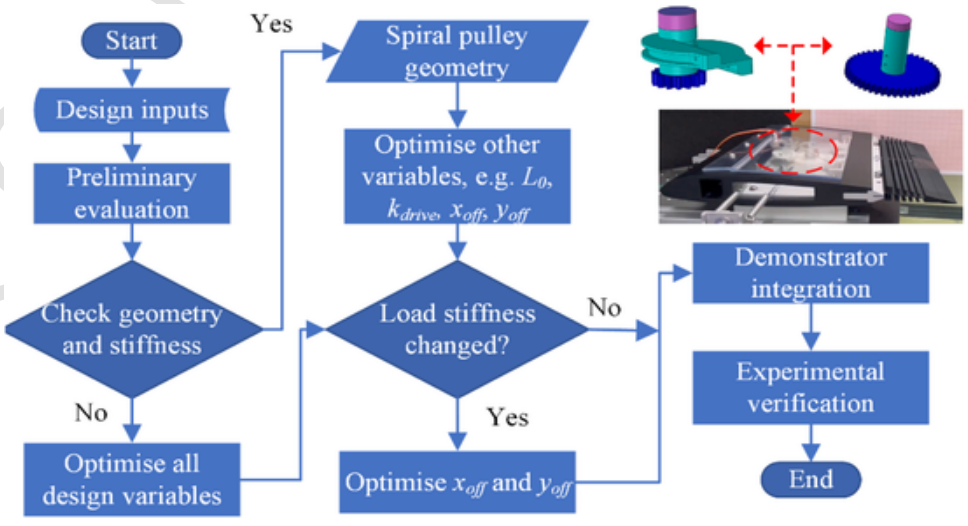

Fig. 4. Workflow of the integration.

sation of all the design variables in Table 2 will be performed for the designated geometry constraints and load stiffness to find a new spiral pulley as performed in the previous research [30].

In the second step, the other parameters of the selected spiral pulley, i.e., the drive spring and installation offsets, will be optimised for the designated load stiffness. Different to previous research [23,30], only some of the design parameters will be tuned and the energy efficiency will be calculated to determine whether the optimisation of partial design parameters is meaningful.

In the third step, the load stiffness will be checked again before final integration. For a varied load stiffness, the installation offsets will be further tuned to improve the energy efficiency, which also provides the basis of applying a mechanism to change the offset adaptively. With all the design variables confirmed, the final integration can be performed, which provides the integrated demonstrator and this is validated experimentally.

In the current study, the workflow will be applied for the integration of the PEB device into the FishBAC morphing structure, while similar procedures can also be applied for other morphing designs.

3. Preliminary evaluation

3.1. Structural stiffness test

Before the optimisation, the load torque required to deform the morphing structure is needed, as the PEB device is designed according to the load stiffness. The required load torque and the corresponding rotation angle was measured as shown in Fig. 5. A simplified demonstrator was built to imitate the integrated situation. A baseline load pulley was installed to transfer the load torque onto the FishBAC structure, and has cables connected to the FishBAC structure at the same position as the practical integrated load pulley. The torque was applied to the structure using a torque wrench with digital output, and the rotation angle was read from the angle gauge connected to the torque wrench.

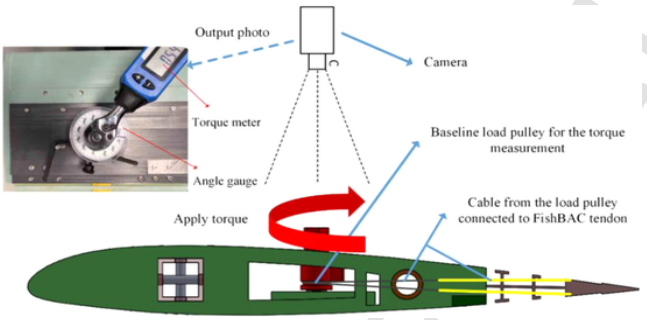

Fig. 5. Schematic of the wing platform for the measurement of the FishBAC structural stiffness.

A camera was placed on top of the experimental setup to record the torque and the angle. An example of the stiffness test is shown in Fig. 5. The FishBAC structure was manufactured by 3D printing. The chord is 270 mm and the span is 250 mm for the convenience of the experiment setup. The printed material has a Young's modulus of approximately 3 GPa.

The required stiffness to deform the FishBAC downward is shown in Fig. 6(a). The deflections of the FishBAC structure are shown in Fig. 6 (b), which represents the downward deflection of the trailing edge. The four pictures demonstrate the trailing edge deflection process when the rotation angle of the load pulley was around 20°. The gear ratio was set to 3 to ensure the rotation of the spiral pulley can reach 60°, which ensures sufficient extension of the drive springs. The load stiffness, k_l, is obtained by dividing the measured torque by the rotation angle of the baseline load pulley, which leads to $k_l = 0.015\text{Nm}/^\circ$. Since the geometry parameters of the load pulley are kept constant in the optimisation of the spiral pulley mechanism, and the load pulley will transfer the torque to the FishBAC structure sequentially, the measured load stiffness can represent the structural stiffness of the FishBAC. In this case, no external loads were added to the structure, and the measured load stiffness only accounts for the structural stiffness of the morphing structure.

The change of the load stiffness can be caused by the use of the structure for different flight conditions and the uncertainties in the process of the manufacturing and assembly. To simplify the estimation, the range of the load stiffness is estimated by evaluating the possible aerodynamic loads on the morphing wing as the total stiffness is mainly determined by the aerodynamic loads on the structure.

Since the current study is limited to static and quasi-static morphing, which does not consider the dynamic response of the morphing wing, XFOIL [32] is used to estimate the loads on the FishBAC wing, which provides the reference value for the estimation. The moment caused by the aerodynamic loads around the hinge axis in the aerofoil, where the FishBAC starts, is obtained as the aerodynamic load torque.

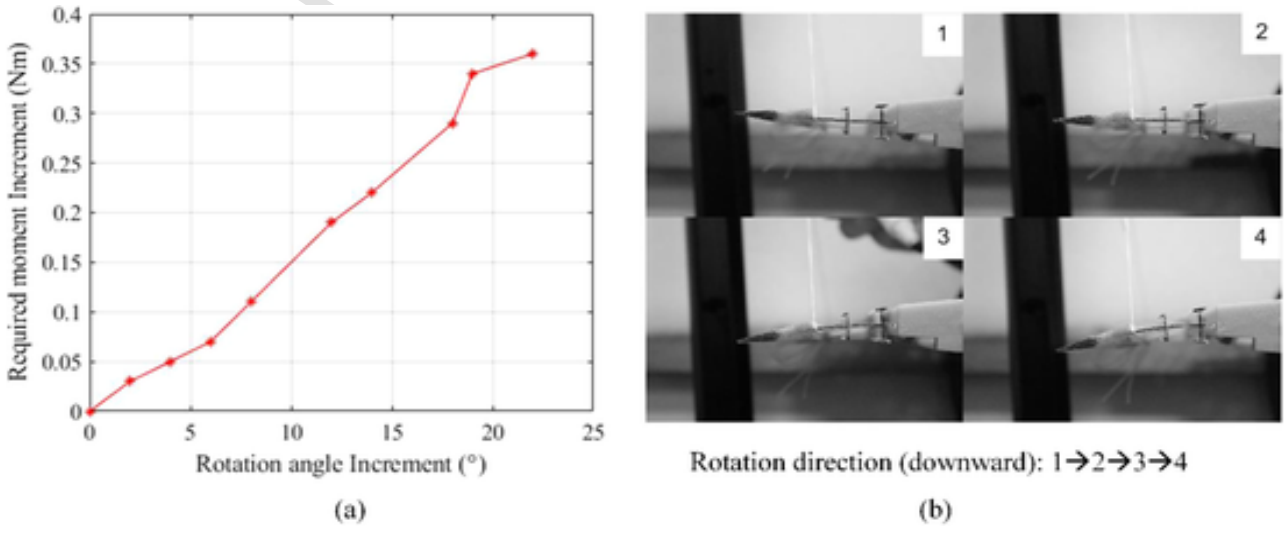

Fig. 6. (a) Required load torque vs the rotation angle of the baseline pulley, (b) Deflections of the FishBAC structure.

The calculated moment is then added to the measured load torque to estimate the range of the load stiffness. In Section 3, the calculation is only used to estimate the stiffness range, which is acceptable for preliminary evaluation in the current study. In a more detailed analysis, the aerodynamic loads changes with the deformation of the morphing wing, and using the hinge moment when the FishBAC wing has no deformation will lead to some errors. In Section 4.3, the fluid structure interaction analysis is performed to show the effect of the aerodynamic loads. The same wing geometry in Section 2 is adopted, and air properties close to those at sea level are adopted. The maximum hinge moment is determined when the angle of attack ranges from −12 to 0 and from 0 to 12° respectively. Suppose the design flight speed ranges from 30 m s^{-1} to 80 m s^{-1}, the load stiffness will vary from 20 % to 180 % of the design point, where $k_l = 0.015$ Nm/° in the current study. The optimised spiral pulley in the previous research [30] corresponds to the load stiffness $k_l = 0.0074$ Nm/°, which is within the estimated range.

Then, the geometry constraints as mentioned in Section 2.2 are checked, which shows the size of the spiral pulley in [30] can satisfy the geometry constraints of the FishBAC wing. Thus, the spiral pully geometry parameters are selected for the integration, which are listed in the fourth column of Table 3.

3.2. Parametric study

A sensitivity analysis of the variables is performed to find the effects of the different parameters. A normalised index Γis defined as

$$\Gamma_i = \frac{S_i}{\sum_{i=1}^{8} S_i}$$
$$S_i = \left| \max\left(J_n\left(D_i\right)\right) - \min\left(J_n\left(D_i\right)\right) \right| \quad i = 1, 2, \ldots 8 \tag{6}$$

where the sensitivity S_i of each variable D_i is calculated by fixing all the other variables according to the first-step results except the variable under consideration. Fig. 7 shows the normalised effect of each variable.

With the bounds listed in Table 3, the sum of the effects of the drive spring and coordinate offsets is much higher than the effect of the spiral pulley geometry. Thus, it might be possible to keep the external energy requirement minimal by only changing the variables related to the drive spring and installation offsets.

Fig. 8 shows the variation of the normalised energy difference J_n when the two variable pairs: (k_{drive}, L_0) and (x_{off}, y_{off}) are changed respectively but the other parameters remain unchanged. To emphasise the trends, the region where J_n is around 1 is shown in the figure. Obviously, the change of the variable pairs will affect the normalised energy requirement significantly.

4. Optimisation and experimental validation

4.1. Optimisation for the specific load stiffness

The same spiral pulley geometry is adopted in the second step, but the load stiffness is obtained in Section 3.1 and is different to that in the first step. The second-step optimisation is performed in MATLAB using a genetic algorithm [33]. The variables in the second step are within the following ranges.

$$\begin{cases} 100 \le k_{drive} \le 1000 \ \text{(N/m)} \\ -0.05 \le L_0 \le 0.4 \ \text{(m)} \\ -50\pi/180 \le \delta_0 \le 50\pi/180 \\ -0.1 \le x_{off} \le 0.1 \ \text{(m)} \\ -0.05 \le y_{off} \le 0.1 \ \text{(m)} \end{cases} \tag{7}$$

The gear ratio is fixed at $g = 3$, and the drive spring initial force is $F_0 = 0$ in this case. The optimised variables are listed in Table 3. The torque output and the energy efficiency of the spiral pulleys are shown in Fig. 9.

Spiral pulley 1 is used for the downward deflection of the FishBAC spine, and spiral pulley 2 is used for the upward deflection, which also corresponds to the positive load pulley rotation. Each of the spiral pulleys can eliminate the corresponding required torque, although the other spiral pulley will also cause a residual torque. The net torque of the bidirectional spiral pulley remains close to zero during the entire load pulley rotation. The optimised spiral pulley can reduce the external energy requirement significantly with the help of the energy stored in the spring, although the opposite drive spring extension will lead to an extra energy requirement.

Fig. 10 shows the variation of the external energy when the normalised load stiffness changes. The x axis corresponds to the load stiffness and the y axis corresponds to the normalised energy difference. The optimised case in the second step has the minimum external energy requirement. When the normalised load stiffness is less than 1, external energy will be used to balance the torque generated by the spiral pulley rather than to deform the structure, which represents energy wasted from the overall system. When the load stiffness is only 20 % of the target design case, over four times of the external energy is required compared to the morphing requirement. On the other hand, when the normalised load stiffness is higher than 1, more external energy is required to deform the morphing structure. But the ratio between the external energy and the morphing requirement remains below 1, which indicates the external energy is still consumed for the structure morphing, rather than for balancing the spiral pulley mechanism, and the rest of the required energy is provided by the passive energy balancing system.

Table 3
Design variables in the design case.

Parameter	lower bound	upper bound	First Step [30]	Second step	Third step	Unit
k_l			0.0074	0.015	Varying	Nm/°
g			1	3	3	-
r_0	-30/1000	10/1000	-0.00828	-0.00828	-0.00828	m
k_1	-0.001	0.02	0.00508	0.00508	0.00508	-
k_2	0	1	0.370	0.370	0.370	-
δ_0	-50*pi/180	50*pi/180	0.505	0.472	0.472	rad
x_{off}	-0.1	0.1	0.014	-0.016	Varying	m
y_{off}	-0.05	0.1	0.042	0.020	Varying	m
L_0	0	0.4	0.20	0.099	0.099	m
k_{drive}	1	1000	69/4	342	342	N/m

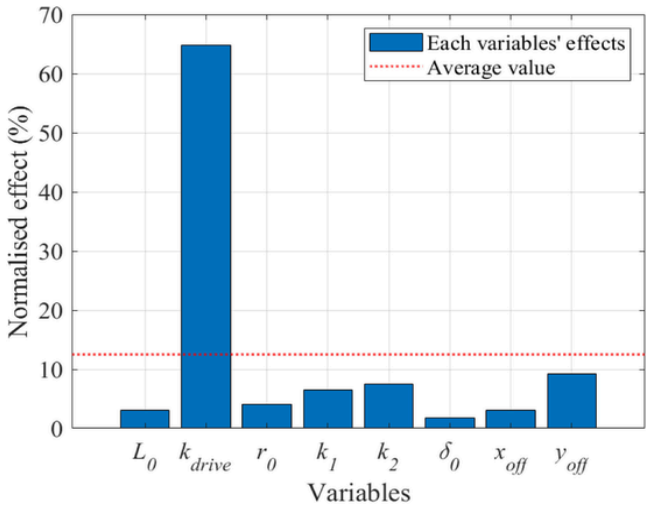

Fig. 7. Contribution of each variable to the performance.

4.2. Effects of varying the spiral pulley installation locations

The results from the second step show that for a specific load stiffness, there might still exist one optimised design point, that can make the energy difference minimum, even if the spiral pulley geometry optimised for another load stiffness is used. However, more external energy is required when the load stiffness varies. In a more general scenario, the variation of the load stiffness should be considered in the design of the passive energy balancing device, especially considering the relatively sophisticated design and manufacturing requirement of the spiral pulley. This can be achieved by further changing the spiral pulley coordinate offsets, x_{off} and y_{off}, adaptively according to the load stiffness. According to Fig. 2, the coordinate offsets are determined by the relative distances between the spiral pulley origin, point O, and the coordinate origin, point A, which inherently represents the installation offset of the spiral pulley origin point. In the passive energy balancing device, the cable that is used to connect the drive spring and the spiral pulley, will go through point A. A short metal pin or a bolt is installed at point A to ensure the cable can pass through that point. As shown in Fig. 8(b), the external energy requirment will be affected when the coordinate offsets x_{off} and y_{off} changes, which makes further optimisation of the offsets for different load stiffnesses reasonable.

The load stiffness is assumed to be linearly increased in the following case. With each load stiffness k_l, all of the other parameters from the second step will remain fixed except the coordinate offsets, x_{off} and y_{off}, which are to be optmised and within the following range:

$$\begin{cases} x^b_{off} - 0.08 \le x_{off} \le x^b_{off} + 0.08 \ \text{(m)} \\ y^b_{off} - 0.08 \le y_{off} \le y^b_{off} + 0.08 \ \text{(m)} \end{cases} \tag{8}$$

where x^b_{off} and y^b_{off} are the optimised results from the second step and relatively large ranges of the offsets are given. A generic algorithm is used for the optimisation. The optimisation starts by only varying one coordinate offset to simplify the mechanism design, and then both of the coordinate offsets are optimised. No constraints are considered.

Fig. 11 shows the variation of the x_{off} and y_{off} respectively when the load stiffness changes.

The load stiffness changes within the range obtained in Section 3.2. The relationship between the offsets and the load stifness is relatively linear in most of the given range, which suggests a linear change of the specific coordinate offset could be made for the corresponding load stiffness. A simple mechanism, such as a worm gear could be adopted to achieve this motion.

When both x_{off} and y_{off} are optimised, the trajectory of point A is drawn in Fig. 12. The results indicate that with an additional mechanism, which can change x_{off} and y_{off} simultaneously, the energy consumption could be further reduced for the specific range of the load stiffness. In this case, the change of x_{off} is not monotonic for the given load stiffness range and thus a more complicated mechanism would be required to achieve the trajectory.

The external energy requirements for the different coordinate offsets are compared in Fig. 13. As different load stiffnesses are used, the actual external energy, E_x, is chosen as the criterion directly rather than the normalized values.

The x axis represents the change of the load stiffness. When the normalised k_l is less than 1, the load stiffness is smaller than the design load stiffness in the second step. But it does not mean less external energy will be required, as the parameters of the mechanism are optimised for that specific load stiffness. More external energy might be needed to overcome the stiffness due to the spiral pulley mechanism itself rather than driving the structure. When the normalised k_l is larger than 1, the load stiffness is higher than that of the design point and will require more external energy if other parameters are fixed.

The red dashed line corresponds to the results from the base solution, which is obtained in the second step and has fixed offsets and the highest external energy requirement when the load stiffness changes.

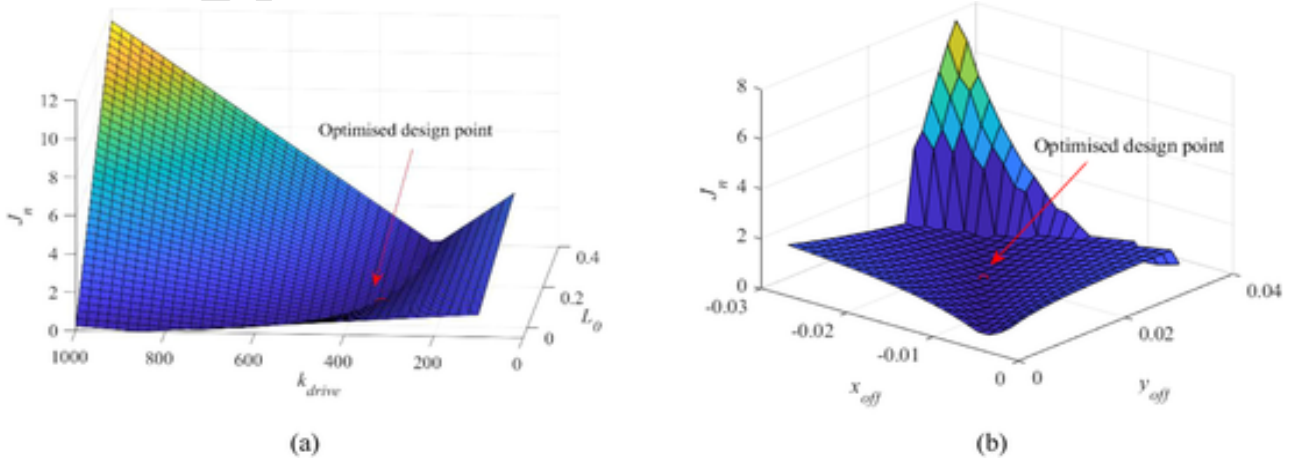

Fig. 8. Influence on the energy requirement of the variable pairs (a): drive spring, (b) installation offsets.

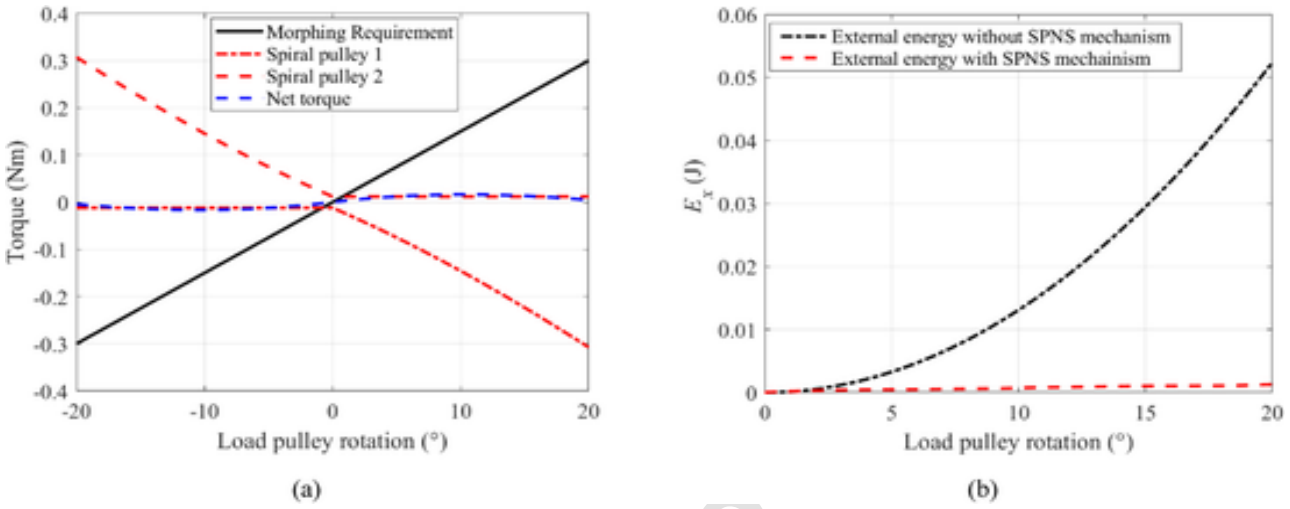

Fig. 9. (a) Torque requirements, (b) Energy consumption.

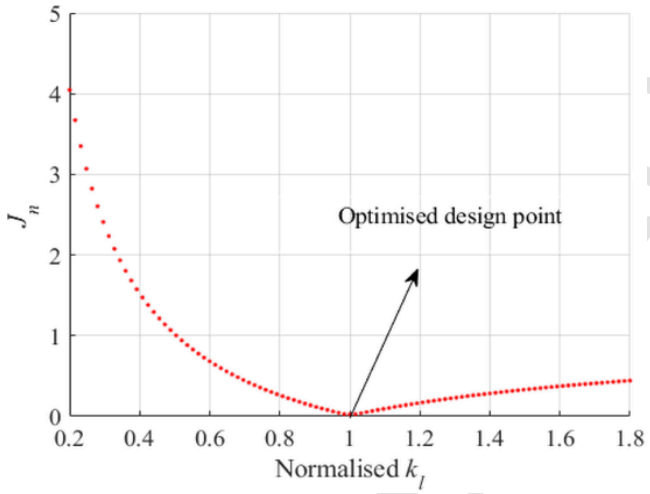

Fig. 10. Influence of the load stiffness on the external energy requirement.

Compared to the base solution, all of the solutions with varying offsets can reduce E_x for the corresponding load stiffness. If only one offset varies, less external energy is required compared to that of the fixed offsets and the required external energy is higher than that of the design point. The least external energy is required when both x_{off} and y_{off} are optimised. In these cases, when the load stiffness is smaller than the design point in the Section 4.1, the external energy is further reduced and becomes even smaller than that of the design point. When the load stiffness is higher than that of the design point, more energy is needed even if both x_{off} and y_{off} are optimised, which means only optimising the offsets but keeping the parameters of the spiral pulley and drive spring fixed is not able to compensate the effect of the higher load stiffness.

4.3. Effects of the fluid structure interaction

To further evaluate the potential of the passive energy balancing device, the fluid structure interaction analysis is performed to obtain the required actuation torque when the aerodynamic loads are applied to the morphing wing.

A static fluid structure interaction scheme is adopted. Since the current study is focused on the actuation system of the morphing wing rather than the high-fidelity aerodynamic analysis, the vortex lattice method and Euler beam method are adopted for the aerodynamic and structural analysis.

Table 1For the preliminary study, a NACA 0012 aerofoil is used in the fluid structure interaction and the chord and span are 305 mm and 150 mm respectively. The FishBAC spine accounts for around 50% of the chord and has the same structural properties in Table 1.The aerodynamic solver is based on XFOIL [32], which is called by MATLAB® [33]. When the aerodynamic loads are needed, a command file will be generated according to the aerofoil shape of the wing, which will be given as the input of XFOIL. The pressure distribution around the aerofoil can be obtained and postprocessed by MATLAB®, and the data are given to the structural solver. The calculation flowchart is shown in Fig. 14.

The structural model is created and calculated based on the Euler beam theory. In-house MATLAB codes are used to calculate the nodal force and moment, which are used to obtain the local nodal deflections and beam cross-section rotation. Due to the presence of the morphing skin, the structural stiffness is non-homogeneous. The aerodynamic loads acting on the wing skin are transmitted to the FishBAC spine via the stringers, so the structure is equivalent to a variable stiffness cantilever beam subjected to multiple concentrated forces and moments.

A similar method was applied in [19], except that the segmental stiffening method [34] is used to obtain the overall deflections of the FishBAC to improve the calculation efficiency. To ensure convergence, a relaxation parameter is included in the fluid structure interaction analysis to reduce the divergent oscillations in the predicted displacements between iterations. The relaxation parameter works by adding numerical damping to the solution, causing the solution to move only partially towards the predicted solution of the next iteration. In this way, forced changes experienced can be reduced, and the tendency for oscillatory solutions leading to diverge can be mitigated.

The actuation loads are applied in the structural model by adding a moment directly to the beam model and the passive energy balancing mechanism is not included in the fluid structure interaction analysis.

In this analysis, the speed of the morphing wing is 40 m s^{-1} and the angle of attack is 5°. Fig. 15(a) shows the iteration process of the trailing edge vertical deflections when different actuation loads are applied. The deflections are nondimensionalised by the wing chord. Fig. 15(b) shows the morphing wing shape when different actuation loads are applied. Both the x and y axis of the are nondimensionalised by the wing chord. The actuation loads correspond to the actuation torque required

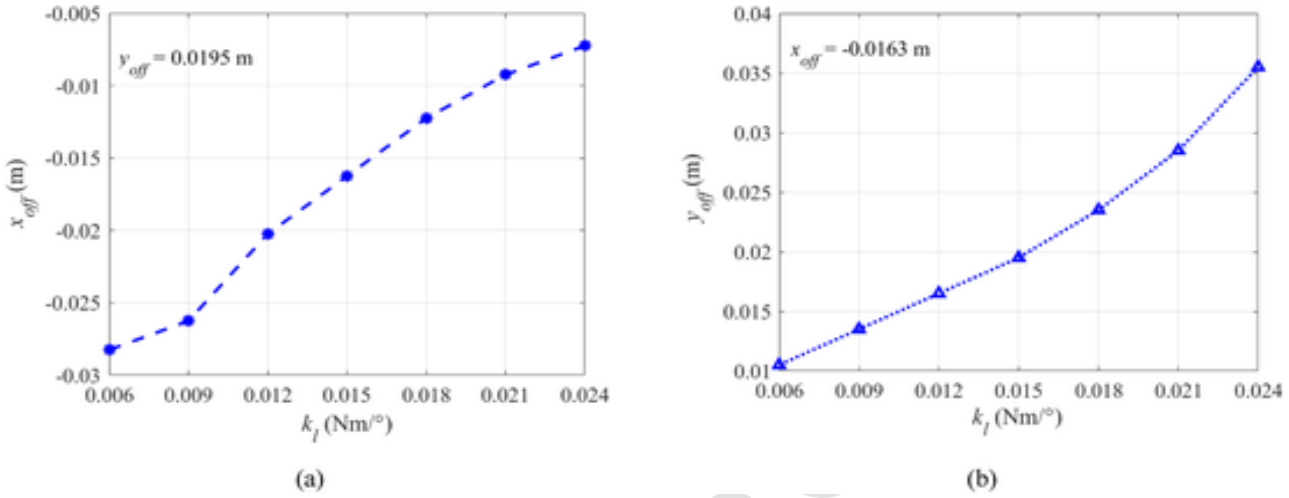

Fig. 11. (a) Variation of x_{off} when k_l changes; (b) Variation of y_{off} when k_l changes.

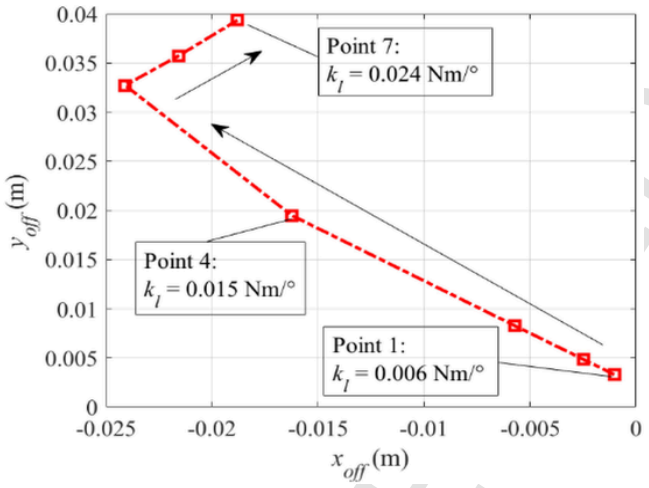

Fig. 12. Trajectory of the spiral pulley offsets when x_{off} and y_{off} are both optimised.

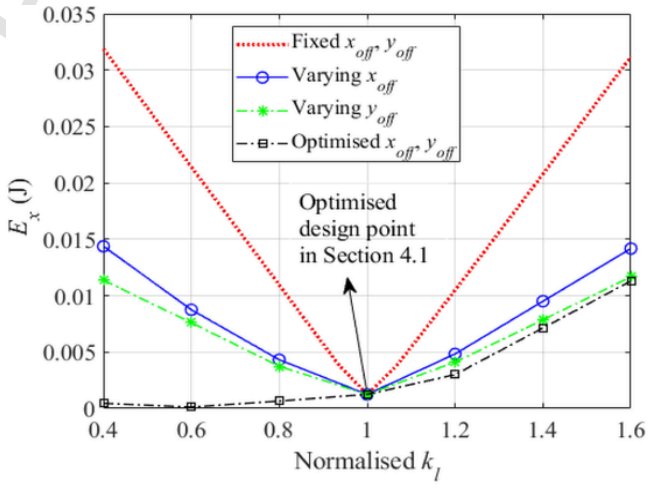

Fig. 13. External energy requirements when the load stiffness changes.

by the different trailing edge deflections, and its energy is provided by the drive springs together with the actuator.

Fig. 16(a) shows the pressure coefficients along the chordwise direction when different actuation loads are applied and the x coordinate is nondimensionalised by the wing chord. To highlight the influence of the aerodynamic loads, Fig. 16(b) compares the required actuation torques in the fluid structure interaction analysis to those when the aerodynamic loads are not considered.

Obviously, higher actuation torques will be required in the fluid structure interaction to overcome the aerodynamic loads. In the current study, the spiral pulley negative stiffness mechanism is designed to balance the structure stiffness, which corresponds to the required actuation torque when the aerodynamic loads are not applied and will be balanced by the PEB device. The rest of the actuation torque will be balanced by the actuator directly. However, when the aerodynamic loads are applied, the actuation torque provided by the actuator can still be reduced by the PEB device since the structural stiffness can still be balanced.

4.4. Demonstrator integration and experimental validation

The optimisation results indicate that the passive energy balancing system could reduce the energy consumption even if the structural stiffness is not as accurate as designed. By varying the location of the spiral pulley, the energy efficiency might be further tuned, which makes the passive energy balancing system more attractive.

A demonstrator was manufactured with the PEB system integrated as shown in Fig. 17(a). Due to the application of different 3D printers, the structural stiffness of the FishBAC structure will be different, which is also used to represent the change of the load stiffness. A similar method to that used in Section 3.1 was applied to measure the structural stiffness, which was estimated as 0.019 Nm/°.

The spiral pulley parameters in the fourth column of Table 3 are still used in the integrated prototype and two slots are further added to change the value of y_{off} when the bolts slide along the slot. A small servo motor is used to actuate the FishBAC structure, as shown in Fig. 17(b), and the deflection of the trailing edge can reach over 4 mm in both upward and downward directions.

Five different cases are tested as summarised in Table 4. Since the load stiffness has changed, optimisation is performed again. In the optimisation, the spiral pulley parameters remain the same as those of the

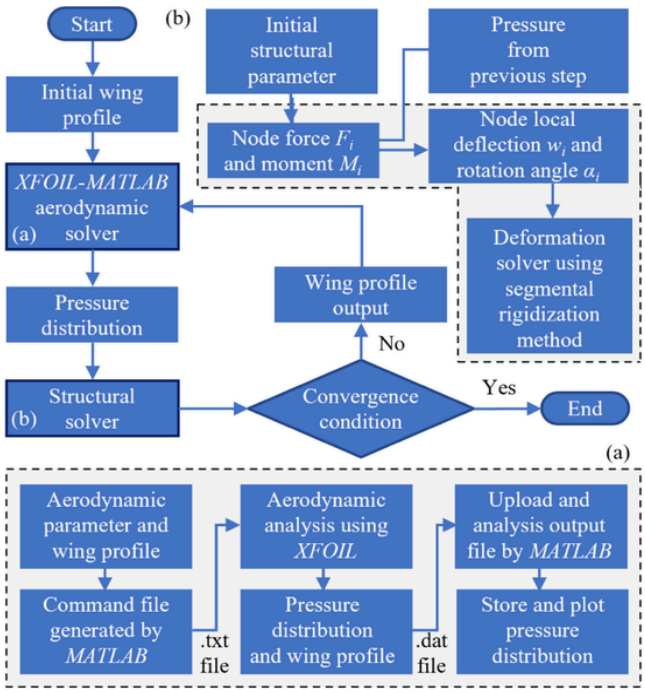

Fig. 14. Flow chat of the fluid structure interaction analysis.

selected candidate [30], and the offsets are optimised together with the drive spring parameters considering the available drive springs. The optimisation leads to the parameters in Case 4. And in Case 1, 2 and 3 the installation offset, y_{off}, is changed linearly to compare the effects on the energy saving. Case 5 corresponds to the situation when the PEB device is not used.

To show the effects of the integration, a current sensor is used to measure the motor currents during operation. The sensor is specially designed with a highly accurate resistor, which will cause a small voltage change due to the working current of the servo motor. The measured current is averaged by calculating the root mean square, and the sampling frequency is 100 Hz during the tests.

Fig. 18(a) shows the measured currents when the servo motor rotates 60° for the downward deflection. It is obvious that with the variation of the offset, the current in the servo motor changes significantly. The servo motor needs to consume a small current even if it is not rotating, and thus the measured energy will not be close to zero compared to the optimisation results in Section 4.1. In the experimental study, Case 4 has the lowest level of current since the corresponding offset is closest to the optimised one. On the contrary, Case 5 needs the highest current as the passive energy balancing system is not working. The currents are then used to calculate the consumed energies. The voltage of the servo motor is 8.4 V and it takes around 2000 ms for the servo motor to reach the stable position during the tests. According to Fig. 18(b), the consumed energy drops from 5.1 J to 2.7 J with a 47 % relative change, which shows the PEB device has the potential to reduce the energy consumption significantly.

To further investigate the effect of the PEB device the currents of the servo motor are also measured when the external load is applied to the demonstrator. The external load is applied by using the weight and pulley, which will be applied to the trailing edge of the camber morphing wing as shown in Fig. 19.

As summarised in Table 5, four cases are further tested with the external loads added. In Case 6 and Case 7, the weight has 200 g, and in Case 8, and Case 9, the weight is increased to 500 g. In Case 6 and Case 8, the PEB device is not adopted while in Case 7 and 9, the PEB device has the optimised variables from Case 4.

Similarly, the current of the servo motor is measured in the additional four cases and the consumed energies are also calculated. Since the external load is applied, it takes more time for the servo motor to reach a stable state and thus the testing time is longer compared to Fig.18. As shown in Fig. 20, due to the higher external loads, the currents in Case 8 and Case 9 will be higher than those in Case 6 and 7 respectively. When the PEB device is used, the current of the servo motor is reduced significantly although the external loads exist.

The energy consumed are shown in Fig. 20(b). Case 7 has the lowest energy consumption since the PEB device is used and the 200 g weight is applied. On the contrary, Case 8 has the highest energy consumption since no PEB device is used and the 500 g weight is applied. Comparing Case 6 to Case 7 and Case 8 to Case 9, around 38 % and 36 % actuation energy can be saved, which is lower than the situations when external loads are applied, but is still a significant reduction.

5. Conclusion

In this paper, passive energy balancing is applied to actuate the FishBAC morphing design. A spiral pulley mechanism is integrated into the FishBAC design and the adaptability of the mechanism for different load stiffnesses is also investigated.

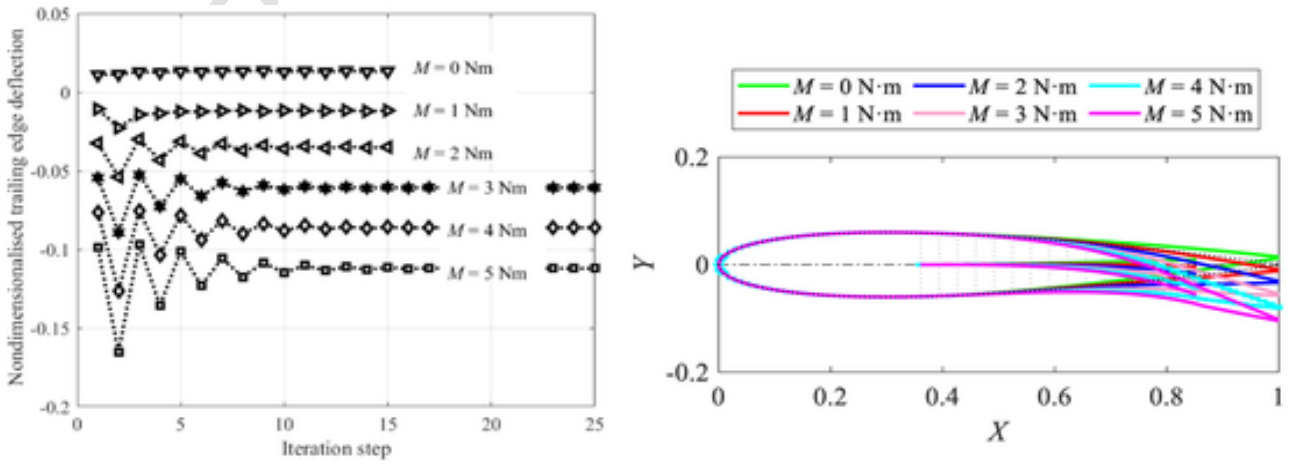

Fig. 15. (a) Trailing edge deflection vs iteration step during the fluid structure interaction analysis, (b) Camber morphing wing shape when subject to different actuation torques.

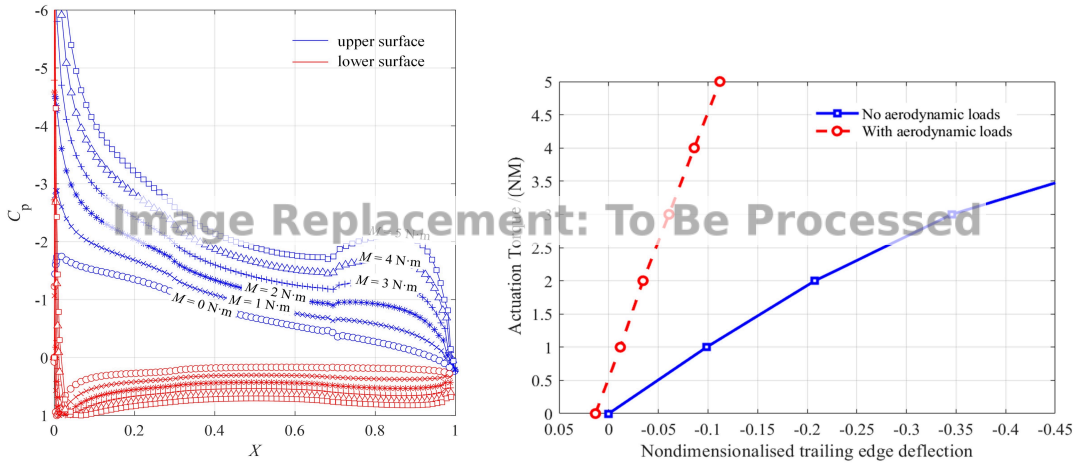

Fig. 16. (a) Pressure distribution obtained from XFOIL, (b) Actuation Torque vs the nondimensionalised trailing edge deflection.

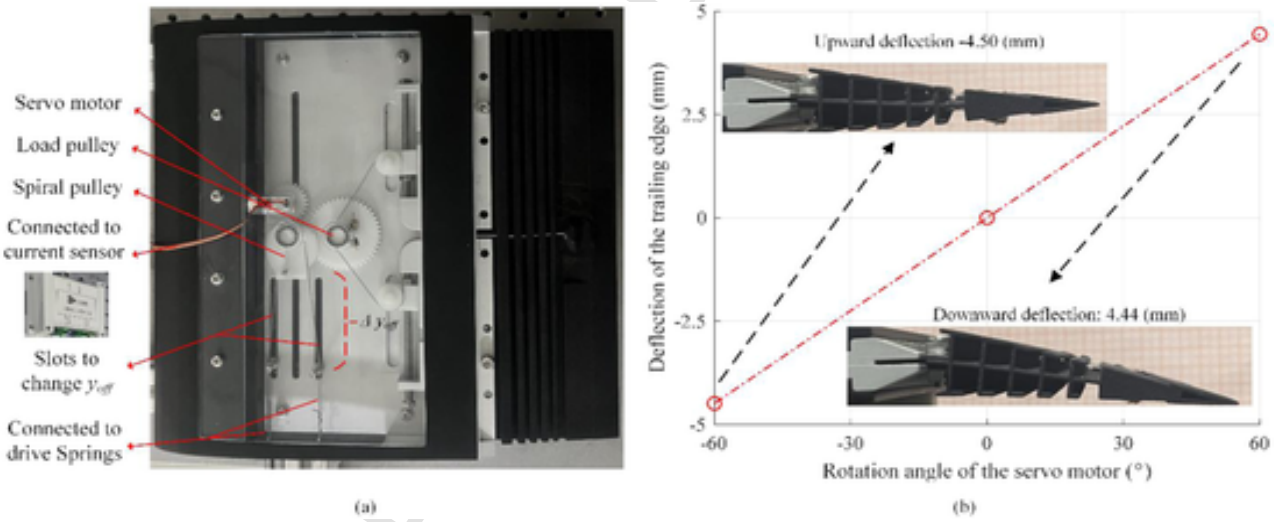

Fig. 17. (a) Integrated demonstrator, (b) Deflection of the trailing edge.

Table 4
Summary of the tested cases with no aerodynamic loads.

Parameters	Case 1	Case 2	Case 3	Case 4	Case 5
k_l	0.019 Nm/°				
g	3				
Spiral pulley parameters	r_0	-0.00828 m			
	k_1	0.00508			
	k_2	0.370			
Drive spring parameters	k_{drive}	312.5 N/m			
	L_0	0.045 m			
x_{off}	0.018 m				
y_{off}	0.09 m	0.03 m	0.06 m	0.048 m	

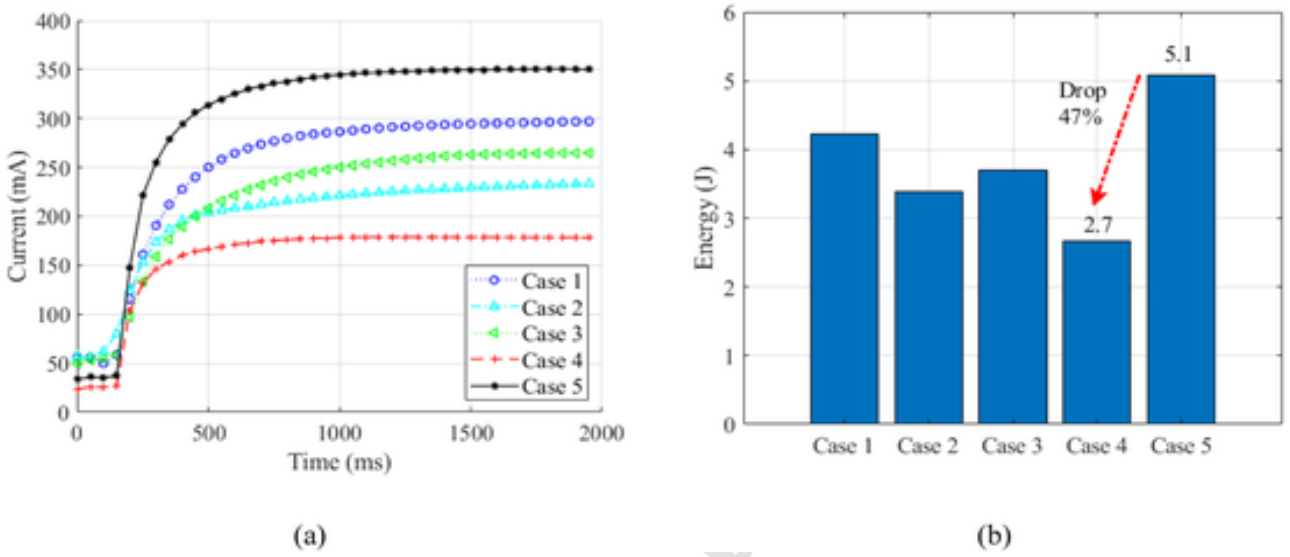

Fig. 18. (a) Measured currents in different cases, (b) Consumed energies corresponding to the different cases.

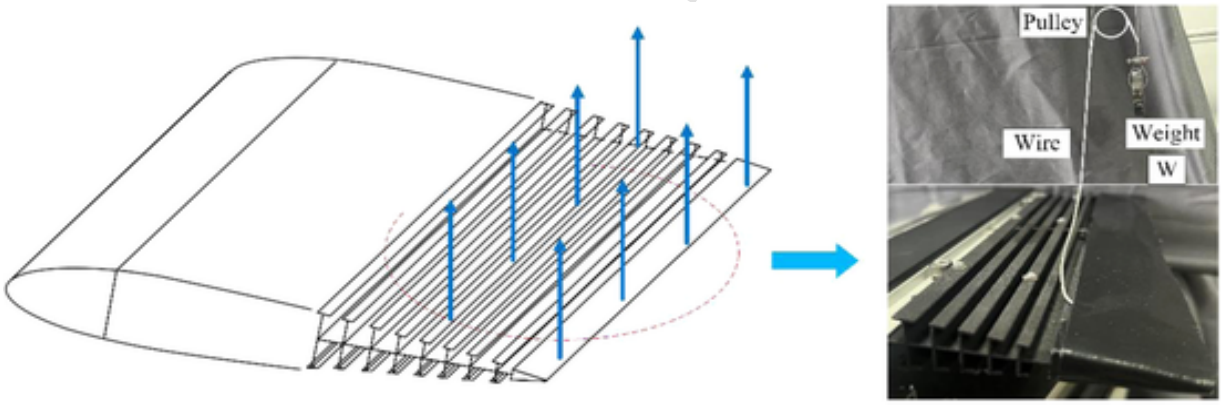

Fig. 19. Demonstrator subject to external loads.

Table 5
Summary of the tested cases with external loads added.

Parameters	Case 6	Case 7	Case 8	Case 9
W	200 g	200 g	500 g	500g
k_l	0.019 Nm/°			
g	3			
r_0		-0.00828 m		-0.00828 m
k_1		0.00508		0.00508
k_2		0.370		0.370
k_{drive}		312.5 N/m		312.5 N/m
L_0		0.045 m		0.045 m
x_{off}		0.018 m		0.018 m
y_{off}		0.048 m		0.048 m

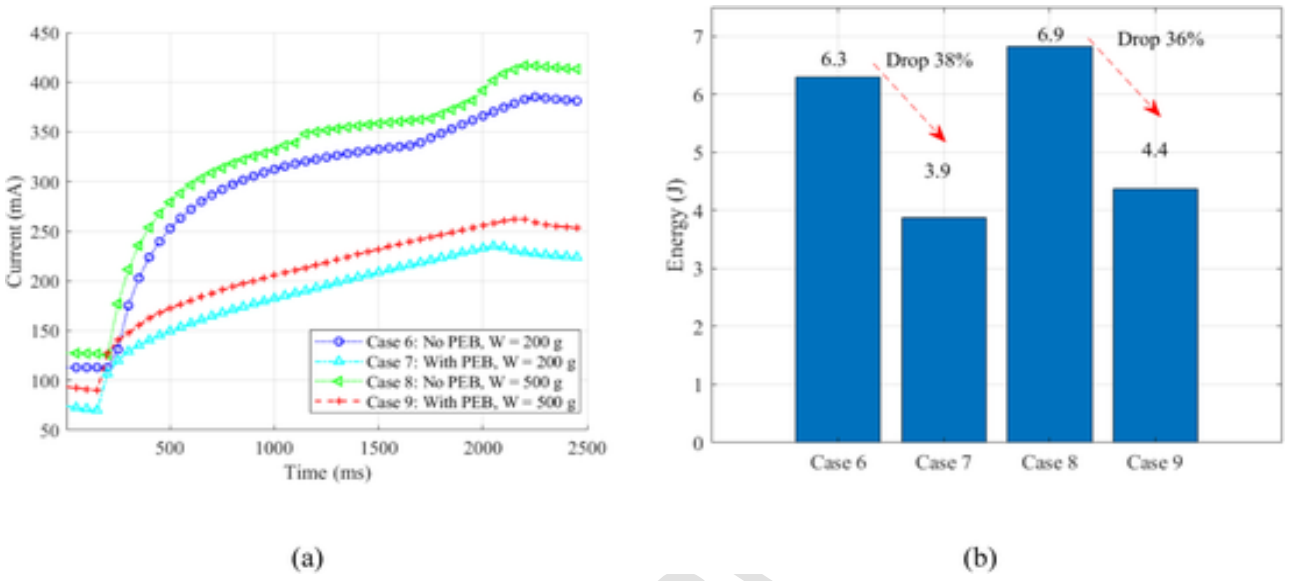

Fig. 20. (a) Measured currents when subject to external loads, (b) Corresponding consumed energies.

A three-step workflow is applied in the paper, after which a demonstrator was built to verify the passive energy balancing concept with both the entire spiral pully mechanism and a servo motor integrated into the FishBAC structure. The following conclusions can be drawn based on the current study:

The passive energy balancing device, including the spiral pulley mechanism and a servo motor, can be integrated into the FishBAC morphing wing structure, and the geometric constraints can be satisfied simultaneously.

(1) Measurement of the working currents in the servo motor shows that the energy required by the morphing structure can be reduced significantly by using the passive energy balancing device, even if external loads are applied to the demonstrator.
(2) By varying the installation offsets of the spiral pulley, the energy efficiency of the system can be tuned and improved even if the structure stiffness changes but the spiral pulley geometry remains unchanged.

The authors understand that the efficiency gains made by this device may in practice be offset by the additional mass of the device itself. In future work, a system level optimisation will be performed, which considers the mass addition due to the passive energy balancing against savings in fuel and actuator mass to identify when the device is likely to give most benefit. Also, in future work, a mechanism can be added to change the installation offset adaptively.

CRediT authorship contribution statement

C. Wang: Writing – original draft. **Y. Zhao:** Writing – review & editing. **K. Huang:** . **J. Zhang:** . **A.D. Shaw:** Validation. **H. Gu:** Investigation. **M. Amoozgar:** Resources. **M.I. Friswell:** Supervision. **B.K.S. Woods:** Methodology.

Declaration of competing interest

The authors declare that they have no known competing financial interests or personal relationships that could have appeared to influence the work reported in this paper.

Acknowledgments

This project has received funding from the European Union's Horizon 2020 research and innovation program under grant agreement No 723491. The first two authors would like to acknowledge the funding from National Natural Science Foundation of China (Grant No 52305262) and the Starting Grant of Nanjing University of Aeronautics and Astronautics (Grant No YQR22056). The third and four author would like to acknowledge the funding from National Natural Science Foundation of China (Grant No 12102017, 92271104) and Beijing Natural Science Foundation (Grant No 1232014).

Data availability

No data was used for the research described in the article.

Supplementary materials

Supplementary material associated with this article can be found, in the online version, at doi:10.1016/j.ast.2024.109641.

Appendix: Derivation of the load torque and drive torque

Table .A1, Fig. A21, Fig. A22, Fig. A23

Table .A1
Summary of the Parameters.

Definition	Parameters	Derivation
Moment arm	l_m	
Spring drive force	F_d	$F_d = \Delta L \cdot k_{drive}$
Gear ratio	g	
Drive torque	T_d	$T_d = g \cdot F_d l_m$
Structure load torque	T_l^s	
Aerodynamic load torque	T_l^a	
Load torque	T_l	$T_l = T_l^s + T_l^a$

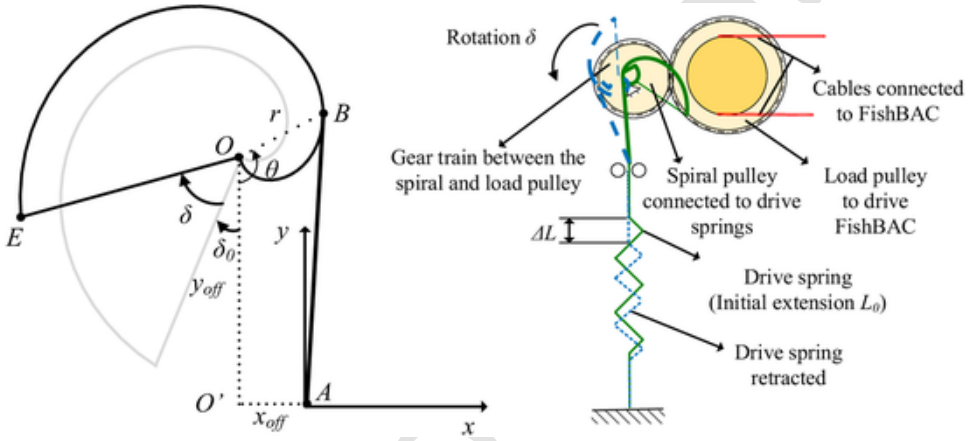

Fig. A21. Geometry of the spiral pulley and its connections to the FishBAC and drive springs.

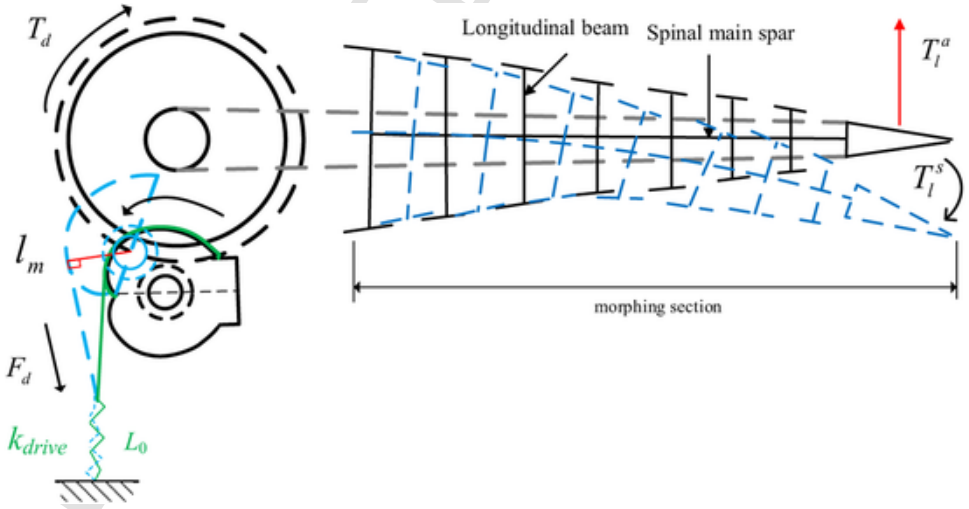

Fig. A22. shows the planar geometry of the spiral pulley and its rotation associated with the drive spring. The radius, *r*, about point O, which is the centre of the rotation shaft, can be defined as an exponential function.

$$r = r_o + k_1 e^{k_2(\theta+\delta+\delta_o)} \tag{9}$$

where δ is the rotation angle of the spiral pulley, θ is an associated angle and δ_0 is the initial rotation angle. The parameters k_1, k_2 are the pre-exponent and exponent terms of the spiral pulley, which will determine the geometry of the spiral pulley together with the initial pulley radius r_0. As shown in Fig. 1, the coordinate offsets of the spiral pulley origin, x_{off} and y_{off}, are also needed to define the location of the spiral pulley.

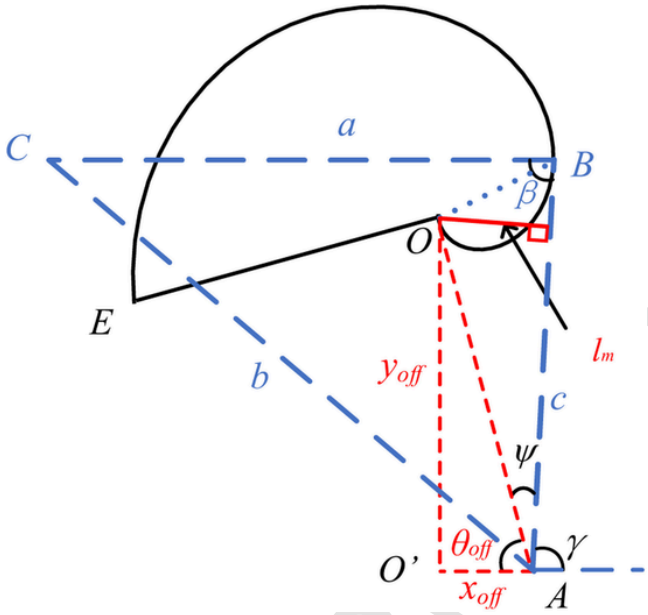

Fig. A23. Geometry of the spiral pulley and its connections to the FishBAC and drive spring.

As shown in Fig. A2, the spiral pulley is connected to the drive spring, which has stiffness k_{drive}, and pre-tension L_0. The spiral pulley is meshed with the load pulley with a gear train to transfer the torque to the FishBAC structure. The load pulley has cables connected to the FishBAC structure, and the drive torque output at the load pulley is given by

$$T_d = g \cdot F_d l_m \tag{10}$$

where g is the gear ratio, F_d is the force caused by the drive spring *and* l_m is the moment arm determined by the geometry feature and the rotation angle of the spiral pulley.

The gear ratio between the spiral pulley and the load pulley is defined as $g = n_2/n_1$, and the number of teeth on the spiral pulley and the load pulley are denoted by n_1 and n_2 respectively. When the gear ratio is larger than 1, the drive torque output by the load pulley can be amplified, which can help to overcome high torque requirements. On the other hand, the rotation angle of the spiral pulley will be increased. The rotation range of the load pulley is determined by the FishBAC structural deformation, which means only a small fraction of the drive spring pre-extension will be used, and most of the stored energy cannot be used to balance the structural deformation. Adding the gears will increase the rotation range of the spiral pulley for the same structural deformation, and increase the efficiency of the passive energy balancing.

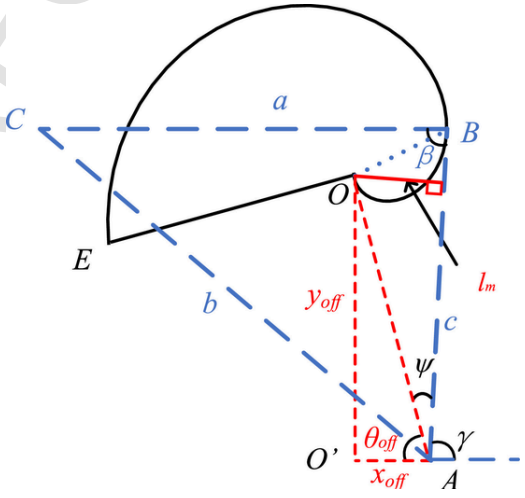

The moment arm, l_m, varies with the rotation of the spiral pulley, and thus the drive torque is influenced by the geometry parameters of the spiral pulley, the drive spring stiffness and the initial extension.

The Cartesian coordinates (with the origin at point A) of any point B along the spiral profile can then be found from:

$$\begin{aligned} x_B &= x_{\text{off}} - r\sin(\pi - \theta) \\ y_B &= y_{off} + r\cos(\pi - \theta) \end{aligned} \tag{11}$$

The length of cable, c, between point B and the origin is equal to:

$$c = \sqrt{x_B{}^2 + y_B{}^2} \tag{12}$$

where a is a fixed, arbitrary length, taken to be 50 mm for this analysis.

$$\begin{aligned} x_C &= x_B - a \\ y_C &= y_B \\ b &= \sqrt{x_C{}^2 + y_C{}^2} \end{aligned} \tag{13}$$

Now that a, b, and c are known, using the cosine law of the triangle ABC one gets

$$\gamma = \beta = \cos^{-1}\left[\frac{a^2 + b^2 - c^2}{2ab}\right] \tag{14}$$

After finding γ and θ_{off}, the arm angle Ψ is

$$\begin{aligned} \theta_{off} &= \tan^{-1}\left(\frac{y_{off}}{x_{off}}\right) \\ \psi &= \pi - \gamma - \theta_{off} \end{aligned} \tag{15}$$

Given the length l_{off} of the vector $A'E$, after finding the arm angle Ψ by the above formula, the arm l_m is

$$\begin{aligned} l_{off} &= \sqrt{x_{off}{}^2 + y_{off}{}^2} \\ l_m &= l_{off} \sin\psi \end{aligned} \tag{16}$$

However, in practice there is only one point that is physically relevant to the unspooling action of the pulley at a given δ, and that is the point at which the straight portion of the cable $\overline{AB}$ leaves tangent to the spiral pulley surface.

The point of tangency occurs when the point C has the minimum corresponding angle γ. The value of θ at the tangent point, $\theta_{min\ \gamma}$, can be solved for by differentiating Eq. (9) with respect to θ and setting equal to zero:

$$\left.\frac{d\gamma}{d\theta}\right|_{\theta_{\min\gamma}} = 0 \tag{17}$$

The drive spring is stretched by an initial amount L_0 so that it may store elastic energy. The force in the drive spring, F_d, can therefore be found from:

$$F_d = \left(L_0 - \Delta L\right) \cdot k_{drive} + F_{off,d} \tag{18}$$

Where k_{drive} is the drive spring constant, and $F_{off,d}$ is the force offset present in the spring. This force offset is a result of the manufacturing method used with extension springs of the type implemented here, and appears as an initial non-linear, high stiffness region in the springs extension before the nominal spring stiffness is achieved. As this force can be considerable, it is important to include it in the analysis.

The arc length, S, of the cable wrapped around the pulley from point B to the cable anchor point, E, can be found from the general form of the arc length formula:

$$\begin{aligned} S &= \int_{\theta(B)}^{\theta(E)} \sqrt{r^2 + \left(\frac{dr}{d\theta}\right)^2}\, d\theta \\ &= \int_{\theta(B)}^{\theta(E)} \sqrt{\left(r_0 + k_1 e^{k_2(\theta+\delta+\delta_0)}\right)^2 + \left(k_2 k_1 e^{k_2(\theta+\delta+\delta_0)}\right)^2}\, d\theta \end{aligned} \tag{19}$$

The total length of cable, L_c is then equal to

$$L_c = b + S \tag{20}$$

The portion of cable that initially lies between point A and the drive spring is not relevant for this analysis since its length is essentially constant, and therefore makes no contribution to the change in length of the drive spring. Instead, the change in drive spring length can be found by subtracting the total cable length evaluated at the current pulley rotation angle, δ, from the total cable length at the initial pulley rotation angle, δ_0, which for this analysis is zero.

$$\Delta L = L_c\left|_{\delta_0} - L_c\right|_{\delta} \tag{21}$$

The load torque, T_l, is required to deform the structure, is given by

$$T_l = T_l^s + T_l^a \tag{22}$$

where the torque caused by the structure is denoted as T_l^s and the torque due to the aerodynamic loads is denoted as T_l^a. In the previous study, only the component T_l^s was considered, which is a fixed function of rotation angle determined by the morphing structure. The component T_l^a due to the aerodynamic loads is determined by the flight conditions.

If the load torque can be balanced by the drive torque partially or completely, less external energy will be consumed by the actuation system, as the energy stored in the drive spring can help to deform the structure. The stiffness corresponding to the load torque is called load stiffness, and denoted as k_l in this paper.

The performance of the passive energy balancing device is evaluated by the energy difference between the energy output of the spiral pulley mechanism and the energy required for FishBAC morphing [19], as the energy difference is inherently provided by the external actuator. The performance index E_x, which is the external energy requirement of the PEB device, is defined as

$$E_x = |E_o - E_r| \tag{23}$$

References

[1] S. Barbarino, O. Bilgen, R.M. Ajaj, M.I. Friswell, D.J. Inman, A review of morphing aircraft, J. Intell. Mater. Syst. Struct. 22 (9) (2011) 823–877.

[2] J. Sun, Q. Guan, Y. Liu, J. Leng, Morphing aircraft based on smart materials and structures: a state-of-the-art review, J. Intell. Mater. Syst. Struct. 27 (17) (2016) 2289–2312.

[3] D. Li, S. Zhao, A. Da Ronch, J. Xiang, J. Drofelnik, Y. Li, L. Zhang, Y. Wu, M. Kintscher, H.P. Monner, A. Rudenko, S. Guo, W. Yin, J. Kirn, S. Storm, R.D. Breuker, A review of modelling and analysis of morphing wings, Progr. Aerosp. Sci. 100 (2018) 46–62.

[4] K. Hu, H. Ge, H. Li, T. Yan, X. Zheng, B. Wang, High actuation capability and smooth-deformation piezo morphing wing based on multi-layer parallel pre-compressed MFC bimorph, Aerosp. Sci. Technol. 132 (2023) 108083.

[5] O. Bilgen, K. Kochersberger, E. Diggs, A. Kurdila, D. Inman, Morphing wing micro-air-vehicles via macro-fiber-composite actuators, in: AIAA 2007-1785. 48th AIAA/ASME/ASCE/AHS/ASC Structures, Structural Dynamics, and Materials Conference, Honolulu, Hawaii, United States, 2007.

[6] J.N. Kudva, Overview of the DARPA smart wing project, J. Intell. Mater. Syst. Struct. 15 (4) (2004) 261–267.

[7] M. DiPalma, F. Gandhi, Bi-directional stiffness for airfoil camber morphing, AIAA J. 56 (4) (2018) 1639–1646.

[8] H. You, S. Kim, W.Y. Joe, G.J. Yun, New concept for aircraft morphing wing skin: design, modeling, and analysis, AIAA J. 57 (5) (2019) 1786–1792.

[9] J. Westfall, R. Canfield, J. Joo, B. Sanders, Multi-disciplinary optimization of a distributed actuation system in a flexible morphing wing. 2007-1715, in: 48th AIAA/ASME/ASCE/AHS/ASC Structures, Structural Dynamics, and Materials Conference, Honolulu, Hawaii, United States, April 2007.

[10] A.C. Henry, G. Molinari, J.R. Rivas-Padilla, A.F. Arrieta, Smart morphing wing: optimization of distributed piezoelectric actuation, AIAA J. 57 (6) (2019) 2384–2393.

[11] Emam, S.A. and D.J. Inman, *A review on bistable composite laminates for morphing and energy harvesting.* Appl. Mech. Rev., 2015. 67(6): p. 060803 (15 pages).

[12] F. Nicassio, G. Scarselli, F. Pinto, F. Ciampa, O. Iervolino, M. Meo, Low energy actuation technique of bistable composites for aircraft morphing, Aerosp. Sci. Technol. 75 (2018) 35–46.

[13] A. Haldar, E. Jansen, B. Hofmeister, M. Bruns, R. Rolfes, Analysis of novel morphing trailing edge flap actuated by multistable laminates, AIAA J. 58 (7) (2020) 3149–3158.

[14] P. Meyer, H. Traub, C. Hühne, Actuated adaptive wingtips on transport aircraft: requirements and preliminary design using pressure-actuated cellular structures, Aerosp. Sci. Technol. 128 (2022) 107735.

[15] J. Sun, L. Du, F. Scarpa, Y. Liu, J. Leng, Morphing wingtip structure based on active inflatable honeycomb and shape memory polymer composite skin: a conceptual work, Aerosp. Sci. Technol. 111 (2021) 106541.

[16] C. Wang, H. Haddad Khodaparast, M.I. Friswell, A.D. Shaw, Y. Xia, P. Walters, Development of a morphing wingtip based on compliant structures, J. Intell. Mater. Syst. Struct. 29 (16) (2018) 3293–3304.

[17] C. Wang, H. Haddad Khodaparast, M.I. Friswell, Conceptual study of a morphing winglet based on unsymmetrical stiffness, Aerosp. Sci. Technol. 58 (2016) 546–558.

[18] J. Zhang, C. Wang, A.D. Shaw, M. Amoozgar, M.I. Friswell, Passive energy balancing design for a linear actuated morphing wingtip structure, Aerosp. Sci. Technol. 107 (2020) 106279.

[19] B.K. Woods, I. Dayyani, M.I. Friswell, Fluid/structure-interaction analysis of the fish-bone-active-camber morphing concept, J. Aircr. 52 (1) (2014) 307–319.

[20] A.E. Rivero, P.M. Weaver, J.E. Cooper, B.K.S. Woods, Parametric structural modelling of fish bone active camber morphing aerofoils, J. Intell. Mater. Syst. Struct. 29 (9) (2018) 2008–2026.

[21] J. Zhang, A.D. Shaw, C. Wang, H. Gu, M. Amoozgar, M.I. Friswell, B.K.S. Woods, Aeroelastic model and analysis of an active camber morphing wing, Aerosp. Sci. Technol. 111 (2021) 106534.

[22] B.K.S. Woods, M.I. Friswell, N.M. Wereley, Advanced kinematic tailoring for morphing aircraft actuation, AIAA J. 52 (4) (2014) 788–798.

[23] B.K. Woods, M.I. Friswell, Spiral pulley negative stiffness mechanism for passive energy balancing, J. Intell. Mater. Syst. Struct. 27 (12) (2016) 1673–1686.

[24] A. Carrella, M.J. Brennan, T.P. Waters, Static analysis of a passive vibration isolator with quasi-zero-stiffness characteristic, J. Sound. Vib. 301 (3) (2007) 678–689.

[25] A. Carrella, M.J. Brennan, I. Kovacic, T.P. Waters, On the force transmissibility of a vibration isolator with quasi-zero-stiffness, J. Sound. Vib. 322 (4) (2009) 707–717.

[26] M. Schenk, S.D. Guest, *On zero stiffness.* Proceedings of the institution of mechanical engineers, Part C, J. Mech. Eng. Sci. 228 (10) (2013) 1701–1714.

[27] M. Schenk, S.D. Guest, J.L. Herder, Zero stiffness tensegrity structures, Int. J. Solids. Struct. 44 (20) (2007) 6569–6583.

[28] S.D. Guest, E. Kebadze, S. Pellegrino, A zero-stiffness elastic shell structure, J. Mech. Mater. Struct. 6 (1–4) (2011) 203–212.

[29] J. Zhang, A.D. Shaw, M. Amoozgar, M.I. Friswell, B.K.S. Woods, Bidirectional torsional negative stiffness mechanism for energy balancing systems, Mech. Mach. Theory. 131 (2019) 261–277.

[30] J. Zhang, A.D. Shaw, A. Mohammadreza, M.I. Friswell, B.K.S. Woods, Bidirectional spiral pulley negative stiffness mechanism for passive energy balancing, J. Mech. Robots 11 (5) (2019), 054502 (7 pages).

[31] J. Zhang, A.D. Shaw, A. Mohammadreza, M.I. Friswell, B.K.S. Woods, Spiral pulley negative stiffness mechanism for morphing aircraft actuation, in: ASME 2018 International Design Engineering Technical Conferences and Computers and Information in Engineering Conference, ASME, Quebec City, Quebec, Canada, 2018.

[32] Drela, M. and Y. Harold. *XFOIL 6.9.* [cited 2020; Available from: https://web.mit.edu/drela/Public/web/xfoil/.

[33] Mathworks, *MATLAB 2019b*. 2019: Natick, MA.

[34] F. Beer, E. Johnston, J. DeWolf, D. Mazurek, Mechanics of Materials, 8th ed, McGraw Hill, New York, 2020.